



Analytical modeling of optical reflectivity of random plasmonic nano-monolayers

ALEJANDRO REYES-CORONADO,^{1*} GESURI MORALES-LUNA,²
OMAR VÁZQUEZ-ESTRADA,³ AUGUSTO GARCÍA-VALENZUELA,² AND
RUBÉN G. BARRERA³

¹Departamento de Física, Facultad de Ciencias, Universidad Nacional Autónoma de México, Ciudad Universitaria, Av. Universidad #3000, Mexico City, 04510, Mexico

²Centro de Ciencias Aplicadas y Desarrollo Tecnológico, Universidad Nacional Autónoma de México, Ciudad Universitaria, Av. Universidad 3000, Apartado Postal 70-186, Ciudad de México, Mexico

³Instituto de Física, Universidad Nacional Autónoma de México, Apdo. Postal 20-364, Mexico City, 01000, Mexico

*coronado@ciencias.unam.mx

Abstract: In this paper, we compare three different models that have been used to interpret reflectivity measurements of supported monolayers of nanoparticles. Two of them: (i) isotropic Maxwell Garnett and (ii) anisotropic two-dimensional-dipolar model are based on an effective-medium approach, while the third one (iii) coherent-scattering model, lies within the framework of multiple-scattering theory. First, we briefly review, on physical grounds, the foundations of each model and write down the corresponding formulas for the calculation of the reflectivity. In the two-dimensional-dipolar model, the dilute limit of the pair-correlation function (also called hole-correlation function) is always used in the calculation of the effective optical response. Then we use these formulas to plot and analyze graphs of the reflectivity of a monolayer of gold nanoparticles on a glass substrate, as a function of several relevant parameters, for two different commonly used experimental configurations. Finally, we discuss the importance of our results and how they can be used to infer the limits of validity of each model.

© 2018 Optical Society of America under the terms of the [OSA Open Access Publishing Agreement](#)

OCIS codes: (160.4760) Optical properties; (260.2110) Electromagnetic optics; (260.3910) Metal optics; (240.6680) Surface plasmons; (240.6380) Spectroscopy, modulation.

References and links

1. X. Yang, H. Yu, X. Guo, Q. Ding, T. Pullerits, R. Wang, G. Zhang, W. Liang, and M. Sun, "Plasmon-exciton coupling of monolayer MoS₂-Ag nanoparticles hybrids for surface catalytic reaction," *Mater. Today Energy* **5**, 72–78 (2017).
2. C. Noguez, "Optical properties of isolated and supported metal nanoparticles," *Opt. Mater.* **27**(7), 1204–1211 (2005).
3. Y. Battie, A. E. Naciri, W. Chamorro, and D. Horwat, "Generalized effective medium theory to extract the optical properties of two-dimensional nonspherical metallic nanoparticle layers," *J. Phys. Chem. C* **118**, 4899–4905 (2014).
4. S. Gwo, C.-Y. Wang, H.-Y. Chen, M.-H. Lin, L. Sun, X. Li, W.-L. Chen, Y.-M. Chang, and H. Ahn, "Plasmonic metasurfaces for nonlinear optics and quantitative SERS," *ACS Photonics* **3**, 1371–1384 (2016).
5. L. Bossard-Giannesini, H. Cruguel, E. Lacaze, and O. Pluchery, "Plasmonic properties of gold nanoparticles on silicon substrates: Understanding Fano-like spectra observed in reflection," *App. Phys. Lett.* **109**, 111901 (2016).
6. K. Kubiak, Z. Adamczyk, J. Maciejewska, and M. Oćwieja, "Gold nanoparticle monolayers of controlled coverage and structure," *J. Phys. Chem. C* **120**, 11807–11819 (2016).
7. G. Hajisalem, Q. Min, R. Gelfand, and R. Gordon, "Effect of surface roughness on self-assembled monolayer plasmonic ruler in nonlocal regime," *Opt. Express* **22**, 9604–9610 (2014).
8. A. Gopinath, S. V. Borisikina, B. M. Reinhard, and L. Dal Negro, "Deterministic aperiodic arrays of metal nanoparticles for surface-enhanced Raman scattering (SERS)," *Opt. Express* **17**, 3741–3753 (2009).
9. Y. Bellouard, E. Block, J. Squier, and J. Gobet, "Plasmon-less surface enhanced Raman spectra induced by self-organized networks of silica nanoparticles produced by femtosecond lasers," *Opt. Express* **25**, 9587–9594 (2017).
10. J. Dai, F. Ye, Y. Chen, M. Muhammed, M. Qiu, and M. Yan, "Light absorber based on nano-spheres on a substrate reflector," *Opt. Express* **21**, 6697–6706 (2013).
11. J. P. López-Neira, J. M. Galicia-Hernández, A. Reyes-Coronado, E. Pérez, and F. Castillo-Rivera, "Surface enhanced Raman scattering of amino acids assisted by gold nanoparticles and Gd³⁺ ions," *J. Phys. Chem. A* **119**, 4127–4135 (2015).

12. T. Okamoto, I. Yamaguchi, and T. Kobayashi, "Local plasmon sensor gold colloid monolayers deposited upon glass substrates," *Opt. Lett.* **25**, 372–374 (2000).
13. O. Vázquez-Estrada, G. Morales-Luna, A. Reyes-Coronado, A. Calles-Martinez, and A. García-Valenzuela, "Sensitivity of optical reflectance to the deposition of plasmonic nanoparticles and limits of detection," *J. Nanophotonics* **10**, 026019 (2016).
14. J. Cao, T. Suna, and K. T. V. Grattana, "Gold nanorod-based localized surface plasmon resonance biosensors: A review," *Sensor Actuat. B-Chem* **195**, 332–351 (2014).
15. X. D. Hoa, A. G. Kirk, and M. Tabrizian, "Towards integrated and sensitive surface plasmon resonance biosensors: A review of recent progress," *Biosens. Bioelectron.* **23**, 151–160 (2007).
16. M. A. García, "Surface plasmons in metallic nanoparticles: fundamentals and applications," *J. Phys. D Appl. Phys.* **44**, 283001 (2011).
17. J. C. M. Garnett, "Colours in metal glasses and meta films," *Philos. Trans. R. Soc. Lond.*, **203**, 368 (1904).
18. L. Bossard-Giannesini, H. Cruguel, E. Lacaze, and O. Pluchery, "Plasmonic properties of gold nanoparticles on silicon substrates: Understanding Fano-like spectra observed in reflection," *App. Phys. Lett.* **109**, 111901 (2016).
19. R. G. Barrera and P. A. Mello, "Statistical interpretation of the local field inside dielectrics," *Am. J. Phys.* **50**, 165–169 (1982).
20. R. G. Barrera, M. del Castillo-Mussot, and G. Monsivais, "Optical properties of two-dimensional disordered systems on a substrate," *Phys. Rev. B* **43**, 13819–13826 (1991).
21. A. García-Valenzuela, E. Gutiérrez-Reyes, and R. G. Barrera, "Multiple-scattering model for the coherent reflection and transmission of light from a disordered monolayer of particles," *J. Opt. Soc. Am. A* **29**, 1161–1179 (2012).
22. L. L. Foldy, "The multiple scattering of waves. I. General theory of isotropic scattering by randomly distributed scatterers," *Phys. Rev.* **67**, 107–119 (1945).
23. H. C. van de Hulst, *Light scattering by small particles*, (Dover Publications, Inc., 1957).
24. C. Sönnichsen, S. Geier, N. E. Hecker, G. von Plessen, J. Feldmann, H. Ditlbacher, B. Lamprecht, J. R. Krenn, F. R. Aussenegg, V. Z.-H. Chan, J. P. Spatz, and M. Möller, "Spectroscopy of single metallic nanoparticles using total internal reflection microscopy," *App. Phys. Lett.* **77**, 2949 (2000).
25. O. Vázquez-Estrada, G. Morales-Luna, A. Calles-Martinez, A. Reyes-Coronado, and A. García-Valenzuela, "Optical reflectivity as an inspection tool for metallic nanoparticles deposited randomly on a flat substrate," *Proc. SPIE* **9556**, 1–9 (2015).
26. L. D. Landau and E. M. Lifshitz, *Electrodynamics of continuous media*, Section 66 (Pergamon, 1969).
27. A. Sihvola, *Electromagnetic mixing formulas*, Eq. (3.5), pp 41 (The Institution of Electrical Engineers, 1999).
28. A. L. Thorneywork, R. Roth, D. G. A. L. Aarts, and R. P. A. Dullens, "Communication: Radial distribution functions in a two-dimensional binary colloidal hard sphere system," *J. Chem. Phys.* **140**, 161106 (2014).
29. L. Tsang and J. A. Kong, *Scattering of electromagnetic waves. Advanced topics*, (John Wiley & Sons, Inc., 2001).
30. R. G. Barrera and A. García-Valenzuela, "Coherent reflectance in a system of random Mie scatterers and its relation to the effective medium approach," *J. Opt. Soc. Am. A* **20**, 296–311 (2003).
31. C. F. Bohren and D. R. Huffman, *Absorption and scattering of light by small particles*, (Wiley-Interscience, 1983).
32. V. A. Loiko, V. P. Dick, and V. I. Molochko, "Monolayers of discrete scatterers: Comparison of the single-scattering and quasi-crystalline approximations," *J. Opt. Soc. Am. A* **15**, 2351–2354 (1998).
33. M. C. Peña-Gomar, J. J. F. Castillo, A. García-Valenzuela, R. G. Barrera, and E. Pérez, "Coherent optical reflectance from a monolayer of large particles adsorbed on a glass surface," *Appl. Opt.* **45**, 626–632 (2006).
34. L. Tsang, J. A. Kong, and R. Shin, *Theory of microwave remote sensing*, (Wiley, 1985).
35. O. Vázquez-Estrada and A. García-Valenzuela, "Reflectivity and transmissivity of a surface covered by a disordered monolayer of large and tenuous particles: theory versus experiment," *Appl. Optics* **56**(25), 7158–7166 (2017).
36. O. Vázquez-Estrada and A. García-Valenzuela, "Optical reflectivity of a disordered monolayer of highly scattering particles: Coherent scattering model versus experiment," *J. Opt. Soc. Am. A* **31**, 745–754 (2014).
37. The so-called reflectivity of a surface corresponds to the collimated-to-collimated reflectance and in general is well approximated by the coherent reflectance of the surface. The difference is that the reflectivity includes all light, the coherent and diffuse components, reaching the detector in a collimated-to-collimated reflectance measurement, whereas the coherent reflectance is calculated only considering the coherent wave and thus, it does not consider that some diffuse light may also reach the detector. However, in practice, the amount of diffuse light captured by the photodetector in a collimated-to-collimated reflectance measurement is negligible.
38. P. B. Johnson and R. W. Christy, "Optical constants of the noble metals," *Phys. Rev. B* **6**, 4370 (1972).
39. C. Noguez, "Surface plasmons on metal nanoparticles: The influence of shape and physical environment," *J. Phys. Chem. C* **111**, 3806–3819 (2007).
40. P. N. Njoki, I.-I. S. Lim, D. Mott, H.-Y. Park, B. Khan, S. Mishra, R. Sujakumar, J. Luo, and C.-J. Zhong, "Size correlation of optical and spectroscopic properties for gold nanoparticles," *J. Phys. Chem. C* **111**, 14664–14669 (2007).
41. http://www.schott.com/d/advanced_optics/ac85c64c-60a0-4113-a9df-23ee1be20428/1.1/schott-optical-glass-collection-datasheets-english-17012017.pdf

1. Introduction

The optical properties of a 2D disordered system of small particles standing on a planar substrate is an interesting topic that has attracted attention, owing to unexpected effects in a system with a relatively simple geometry [1–6], and also due to possible practical applications [7–16]. We will refer to this system as a *colloidal monolayer*, or simply as a *monolayer*, and we will concentrate here in the calculation and analysis of the reflection amplitudes from an incident plane wave. In this paper we address three available analytical models to calculate the reflectivity of a surface partially covered by a disordered monolayer of spherical particles. These models require simple calculations and could readily be used in several applications. In our analysis we consider simple supported plasmonic nano-monolayers which are of current interest in many areas of physics, both fundamental and applied. From the approximations used to derive each of them one can infer some of their limitations, but their applicability limits are not well established. In fact, since the physical assumptions behind the three models differ markedly, one could even question the applicability of any of them based on the other two. One could compare predictions by these models with experiments or with “exact” numerical simulations. But a first step in exploring their validity is to compare, among themselves, their predictions for identical systems. A second objective of this paper is to provide results to identify within a wide range of surface coverages, particle sizes, and a broad band of incident frequencies some attractive examples for experimental or numerical verification.

We start with the effective-medium approach and the widely used Maxwell Garnett model (MGM) [17], because it is commonly applied to the interpretation of experimental data coming not only from composite bulk materials and colloidal suspensions, but also from low-dimensional systems like monolayers of particles on a substrate [18]. Although it has been recognized that MGM is a model valid for a system of identical spheres randomly located within a homogeneous material in 3D, it has been frequently applied also to 2D systems [18]. This is probably because it relates, in a simple manner, the effective dielectric response to the polarizability of the spheres and their volume filling fraction. In MGM, the spheres are assumed to be polarizable and small enough, so in the presence of an external electromagnetic field, the induced fields they generate outside the spheres can be regarded as dipolar fields whose origin is located at the center of the spheres. Nevertheless, the field that excites each sphere can be calculated, approximately, by considering that each sphere is surrounded by the rest of the spheres, regarding them as equally polarized with the average dipole moment, and randomly located in 3D homogeneously and isotropically “on the average” [19]. It is therefore questionable to apply this model to a monolayer system in which one expects, from the start, an anisotropic effective dielectric response—different in the directions along and perpendicular to the plane of the monolayer—.

A model that heals all the above-mentioned shortcomings of MGM for 2D disordered systems, keeping the same kind of approximations and leading also to very simple formulas for the anisotropic components of the effective dielectric-response tensor, is what we call the 2D dipole model (2D-DM) [20]. In this model one also considers that, in the presence of an external field, the induced fields outside the spheres are strictly dipolar. The field that excites each sphere is also regarded as coming from all other spheres in the monolayer, all evenly polarized—mean-field approximation—but located only on the plane of the monolayer. In addition, the contribution to the exciting field coming from the surface charge due to the surface charge induced on the substrate, is also included. This induced surface charge is regarded, in the quasistatic approximation, as coming from the image of the dipolar charge induced in the spheres, that we call, the image dipoles. This model could be regarded as the 2D version of MGM, and due to the way the exciting field is calculated, it is expected to be valid up to a rather large surface coverage.

The third model that we will consider here is not within the effective-medium approach but rather within the so-called multiple-scattering theory, and we will refer to it as the coherent scattering model (CSM) [21]. The CSM assumes that the exciting field at each identical sphere is

given by the macroscopic—average—field, but the field scattered by each sphere goes beyond the dipolar moment, and takes account of all multipolar orders providing, nevertheless, a simple formula for the reflection amplitudes in terms of the elements of the scattering matrix of each individual sphere. Since the exciting field is taken as the average field, this model will be valid only for low surface coverages, but due to the inclusion of all multipoles in the scattering process, it will be valid for both small and large particles. This approximation is similar to the one proposed by Foldy [22] and van de Hulst [23] for the 3D case. However note that here we deal with a quite different system: a 2D monolayer of identical spheres on a substrate.

It is also our objective to compare the three aforementioned models as a function of the relevant parameters of the problem: particle size, surface coverage, angle of incidence and wavelength of the incident radiation; studying the regions where their assumed validity overlaps (very small particles and low surface coverage), and analyzing the situations where they depart from each other, as either the particle size or the surface coverage increases. To be aware of the effects of the particulate structure of the monolayer, in our comparisons we also include reflectivity calculations for a homogenous thin film with the same amount of material as in the particulate monolayers.

We will present results for two different experimental set-ups: (i) one called internal incidence, when the monolayer is illuminated from the substrate side, that will be assumed to be a transparent prism, and (ii) the other called external incidence, when the monolayer is illuminated from the monolayer side. The main advantage of internal incidence is that a prism with a high enough index of refraction might give rise to a critical angle [24], and we showed that this set increases vastly the sensitivity of measurements at angles of incidence around the critical angle [13, 25].

The paper is organized as follows: In Section 2 we review the effective-medium models: the Maxwell Garnett model (MGM) and the 2D dipole model (2D-DM), and in Section 3 we present a brief summary of the coherent scattering model (CSM). In Section 4 we compare and analyze the results obtained from the three different models: MGM, 2D-DM and CSM, as well as the ones predicted by an effective homogeneous thin film, and Section 5 is devoted to a discussion of our results and to explore different experimental configurations that could be adequate to further explore the validity of the above mentioned models. Finally, in Section 6 we summarize our findings and highlight our conclusions.

2. Effective-medium approach

The objective of an effective-medium approach to the optical properties of a given system is to devise a medium with effective properties, in our case, an effective permittivity and an effective permeability, such that the sources—induced charges and induced currents—and the induced fields—electric and magnetic—are the same as the ones given by the average of the sources and fields generated by the actual system. By average we mean any process that smooths out the rapid spatial variations of the sources and the fields up to a certain characteristic length, yielding the total field as the sum of the smooth component—average—plus the rest—fluctuations—. But, since we deal only with macroscopic (average) fields, we will ignore the field fluctuations.

The effective-medium formalism used here includes two previously developed models: the well-known Maxwell Garnett model [17] and the 2D dipole model [20]. We provide a brief summary of the calculation of the effective dielectric response of a monolayer, for these two models, together with the corresponding expressions for the reflection amplitudes obtained by using Fresnel's formulas. For the MGM we will only write down the well-known formula for the effective dielectric response together with some comments about its derivation and validity. In case of the 2D dipole model (2D-DM), we will review briefly the derivation of the components of the effective dielectric response tensor of the monolayer, emphasizing the main assumptions that limit its validity, and then describe how can one use this effective dielectric response in Fresnel's three-layer formula [26], to obtain the reflection and transmission amplitudes for internal and

external incidence.

2.1. Maxwell Garnett model

As mentioned in the introduction, the MGM considers a system of identical non-magnetic polarizable spheres with permittivity ϵ_p , randomly located within a homogeneous non-absorptive medium—the matrix—with permittivity ϵ_m . The field exciting each sphere—local field—is calculated by assuming that the dipole moment induced in all other spheres, is the average dipole moment. In other words, one neglects the fluctuations of the polarization field. The effective permittivity is given by (see for example [27])

$$\frac{\epsilon_{\text{MG}}^{\text{eff}}}{\epsilon_m} = \frac{\epsilon_p (1 + 2f) + 2\epsilon_m (1 - f)}{\epsilon_p (1 - f) + \epsilon_m (2 + f)}, \quad (1)$$

where $f = Nv_p/V$ is the volume filling fraction of the N spheres; here v_p is the volume of one sphere and V is the total volume of the system. Two things are worth noting about this expression. First, $\epsilon_{\text{MG}}^{\text{eff}}$ does not depend on the size of the spheres, the only requirement is that they are small in relation to the wavelength of the incident external field. Second, $\epsilon_{\text{MG}}^{\text{eff}}$ does not depend on statistical distribution of spheres, in particular, it does not depend on the pair-correlation function. This second fact might seem puzzling, because the interaction between dipoles is given through a two-point operator and the configurational average of any two-point operator requires the pair-correlation function as a weighting function. The independence of $\epsilon_{\text{MG}}^{\text{eff}}$ on the pair-correlation function is actually due to a mathematical “accident” that happens only in the very special case of a system of particles interacting—in 3D—through dipolar forces, with an isotropic pair-correlation function, as it has been shown already in [19]. When this formula is applied to a 2D system, as in the case of a monolayer, the effective medium is regarded naively as a slab of area A and height $d = 2a$, where a is the radius of the spheres, with the only precaution of taking $f = (2/3)\Theta$, where $\Theta = N\pi a^2/A$ denotes the surface coverage.

2.2. 2D dipolar model

This model yields the calculation of the effective optical parameters of a monolayer of randomly located particles on top of a substrate, by regarding the monolayer-substrate system as an “effective” continuous film. Here we are interested in the reflection and transmission amplitudes of an incident monochromatic plane wave on the monolayer-substrate system. If we further assume that the monolayer and the substrate are both non-magnetic, then one requires to devise only an effective permittivity—and not an effective permeability—and then use it in the formalism of continuous electrodynamics, as if it were a film of an ordinary material. One may wonder why do we consider the effective medium as a system composed by the monolayer and the substrate and not by the monolayer by itself, that is, self-standing. The reason is that in this model, as mentioned in the Introduction, one is looking for the field that excites the spheres on the substrate, assuming the induced dipole in all the spheres is equal and given by the average dipole. An important contribution to the exciting field comes not only from the near field, of the neighboring spheres, but also from the field of their image dipoles induced on the substrate; in a self-standing monolayer this local effect will be missing. The replacement of the surface charge induced on the substrate, by a discrete set of image dipoles, assumes the validity of the quasistatic approximation; this is justified, because the main contribution of the induced surface charge to the exciting field on a given sphere, comes from the self-image and the image dipoles that are closest to it, and all these are located at distances much less than the incident wavelength.

We consider also that the thickness of the “effective” film is much less than the wavelength of the incident plane wave, thus one expects the effective permittivity to be anisotropic, because the polarization process within the monolayer should be different in the directions parallel and

perpendicular to the substrate. One defines the effective electric susceptibility tensor $\overleftrightarrow{\chi}^{eff}$ as the relation between the macroscopic (average) polarization field \vec{P} and the macroscopic (average) electric field \vec{E} , that is,

$$\vec{P} = \epsilon_0 \overleftrightarrow{\chi}^{eff} \cdot \vec{E}, \quad (2)$$

where ϵ_0 is the permittivity of vacuum, $\overleftrightarrow{\chi}^{eff} = \text{diag}[\chi_{||}^{eff}, \chi_{||}^{eff}, \chi_{\perp}^{eff}]$, the subscripts $||$ and \perp denote directions parallel and perpendicular to the substrate, and we have further assumed, that on the average, the monolayer is isotropic in directions parallel to the substrate. We are using SI units. Now, in continuous electrodynamics the relationship between the effective electric susceptibility $\overleftrightarrow{\chi}^{eff}$ and the effective dielectric response $\overleftrightarrow{\epsilon}^{eff}$ is given by $\overleftrightarrow{\epsilon}^{eff} = \epsilon_0 (\overleftrightarrow{I} + \overleftrightarrow{\chi}^{eff})$, where \overleftrightarrow{I} is the unit tensor.

The idea now is to set up a mathematical model for the monolayer of particles on the substrate in the presence of an external electric field oscillating at frequency ω , then calculate the average induced dipole per unit volume and determine its relation with the average electric field \vec{E} within the monolayer, in order to identify $\overleftrightarrow{\chi}^{eff}$. Notice that the calculation of \vec{P} and \vec{E} requires the introduction of a characteristic thickness d of the monolayer. Since the calculation of the average electric field \vec{E} within the monolayer is not straightforward, we will first derive below an approximate relationship between \vec{E} and the external field \vec{E}^{ext} that will greatly simplify the calculation of the effective response.

We first recall that at a planar interface the components of the electric field parallel to the interface $E_{||}$, and the components of the displacement field perpendicular to the interface D_{\perp} , must be continuous, thus if we consider that the “effective” film is so thin that one can assume that $E_{||}$ and D_{\perp} do not change appreciably within the film, then one obtains a relationship between macroscopic field \vec{E} within the film and the field outside the film, that we will call the external field, thus

$$\left(E_{||}, \epsilon_{\perp}^{eff} E_{\perp} \right) \approx \left(E_{||}^{ext}, \epsilon_m E_{\perp}^{ext} \right), \quad (3)$$

where we have now assumed that the medium on top of the monolayer is not vacuum but rather a non-absorptive material with permittivity ϵ_m , and it is from where the incident wave is coming (external incidence). Actually, what we call here the external field is the incident field plus the field reflected by the surface of the bare substrate, without the monolayer. We now assume that the material on top of the monolayer is the same as the material outside the spheres within the monolayer, and then use Eq. (3) together with

$$\vec{P} = \epsilon_m \overleftrightarrow{\chi}^{eff} \cdot \vec{E} \quad (4)$$

and $\epsilon_m \overleftrightarrow{\chi}^{eff} = \overleftrightarrow{\epsilon}^{eff} - \epsilon_m \overleftrightarrow{I}$, to write the parallel and perpendicular components of the polarization field, in terms of the components of the macroscopic electric field, that is,

$$P_{||} = \left(\epsilon_{||}^{eff} - \epsilon_m \right) E_{||}^{ext}, \quad (5)$$

$$P_{\perp} = \left(1 - \frac{\epsilon_m}{\epsilon_{\perp}^{eff}} \right) \epsilon_m E_{\perp}^{ext}. \quad (6)$$

We now formulate a model to calculate \vec{P} , by first regarding the monolayer as a collection of $N \gg 1$ non-magnetic identical spheres randomly located, embedded in a non-absorptive material with permittivity ϵ_m and sitting on top of planar non-magnetic substrate with permittivity ϵ_s ; the spheres have a radius a and permittivity ϵ_p . The substrate is regarded as a half space ($z < 0$) and the position of the center of the particles on the XY plane is denoted by \vec{R}_j . The system is set on

the presence of an arbitrary external field \vec{E}^{ext} that oscillates at frequency ω and polarizes the particles with wavelength λ , much larger than the typical separation between particles. The main assumption is that on each particle a dipole moment \vec{p}_i is induced, and it is given by

$$\vec{p}_i = \epsilon_m \alpha_{pol}(\omega) \left[\vec{E}^{ext} + \sum_{j \neq i}^N \overleftrightarrow{t}_{ij} \cdot \vec{p}_j + \sum_j^N \overleftrightarrow{t}_{ij}^I \cdot \overleftrightarrow{M} \cdot \vec{p}_j \right], \quad (7)$$

where α_{pol} is the frequency-dependent polarizability of the particles, further assumed to be isotropic, and the expression in square brackets is the electric field that polarizes the i -th particle, the so-called local (exciting) field. This local field is given by the sum of three terms: the first term is the external field \vec{E}^{ext} , the second term is the field generated by all the induced dipoles, but the i -th one ($j \neq i$), and the third term is the field coming from the charges and currents induced on the substrate. This induced field is calculated in the quasistatic approximation—radiation corrections are neglected—as the fields generated by the dipoles induced in all other spheres and their images, including the self-images; the geometry is illustrated in Fig. 1. Here, $\overleftrightarrow{t}_{ij} = \nabla_i \nabla_j (1/R_{ij})$ corresponds to the dipole-dipole interaction tensor, and $\overleftrightarrow{t}_{ij}^I = \nabla_i \nabla_j (1/R_{ij}^I)$ corresponds to the dipole-image dipole interaction tensor, with $\vec{R}_{ij}^I = \vec{R}_{ij} - 2a \hat{a}_z$ denoting the vector from the image of the j -th particle to the i -th particle. Here $\overleftrightarrow{M} = A \text{diag}(-1, -1, 1)$, with $A = (\epsilon_s - \epsilon_m)/(\epsilon_s + \epsilon_m)$, takes account of the strength and direction of the image dipole.

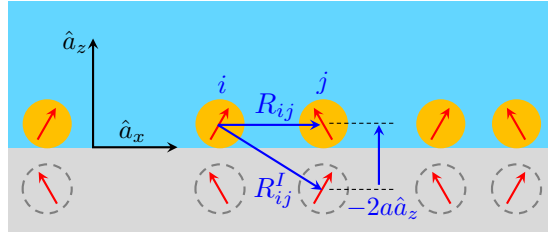


Fig. 1. Schematics of the supported spherical particles (yellow circles) forming the monolayer and their images induced in the substrate (gray-dashed circles).

Now, one has to solve Eq. (7) for $\{\vec{p}_i\}$ with $i = 1 \dots N$, in terms of \vec{E}^{ext} , then take an average to obtain the average dipole moment $\langle \vec{p} \rangle$ which can be related to the macroscopic polarization vector through $\vec{P} = N \langle \vec{p} \rangle / V$, where V is the volume of the monolayer, and finally identify $\overleftrightarrow{\epsilon}^{eff}$ using Eqs. (5) and (6). We do this in the Mean-Field Approximation (MFA), that is, one substitutes \vec{p}_j by $\langle \vec{p} \rangle$ in Eq. (7), then take an average of the resulting equations, and one gets

$$\langle p_x \rangle = \epsilon_m \alpha_{pol} \left[E_x^{ext} + \sum_j^N \langle \overleftrightarrow{u}_{ij}^{xx} \rangle \langle p_x \rangle \right], \quad (8)$$

$$\langle p_z \rangle = \epsilon_m \alpha_{pol} \left[E_z^{ext} + \sum_j^N \langle \overleftrightarrow{u}_{ij}^{zz} \rangle \langle p_z \rangle \right], \quad (9)$$

where $\overleftrightarrow{u}_{ij} = (1 - \delta_{ij}) \overleftrightarrow{t}_{ij} + \overleftrightarrow{t}_{ij}^I \cdot \overleftrightarrow{M}$ and the averaging procedure considered here will be an ensemble average over different configurations of the randomly located particles. We will also restrict ourselves to isotropic ensembles with translational invariance, so the average obtained in this way will be independent of position, and also $\langle p_x \rangle = \langle p_y \rangle$.

The next step is to calculate the averages of the components of the tensor $\overleftrightarrow{u}_{ij}$, solve for $\langle p_x \rangle$ ($= \langle p_y \rangle$) and $\langle p_z \rangle$ in terms of E_x^{ext} and E_z^{ext} , then calculate the components of the polarization vector $P_x = N \langle p_x \rangle / V$ and $P_z = N \langle p_z \rangle / V$, and using Eqs. (5) and (6) one obtains finally expressions for ϵ_{xx}^{eff} ($= \epsilon_{yy}^{eff}$) and ϵ_{zz}^{eff} . Before displaying the results of this calculation, let us point out that in the computation of the configurational average of the components of $\overleftrightarrow{u}_{ij}$ the radial distribution function (also called pair-correlation function) $\rho^{(2)}(R_{ij})$ should come out, because being $\overleftrightarrow{u}_{ij}$ a two-point function, one requires to know the probability of finding a particle at \vec{R}_j given one fixed at \vec{R}_i . The final expressions obtained, within the MFA, for the effective permittivity of a disordered monolayer of identical spheres on the top of a substrate, are given by [20]

$$\frac{\epsilon_{xx}^{eff}}{\epsilon_m} = 1 + \frac{2\Theta\tilde{\alpha}_{pol}}{1 - A\frac{\tilde{\alpha}_{pol}}{8} - \Theta\tilde{\alpha}_{pol}\frac{1}{2}(G - AG^I)}, \quad (10)$$

$$\frac{\epsilon_m}{\epsilon_{zz}^{eff}} = 1 - \frac{2\Theta\tilde{\alpha}_{pol}}{1 - A\frac{\tilde{\alpha}_{pol}}{4} + \Theta\tilde{\alpha}_{pol}(G + AG^I)}, \quad (11)$$

where Θ is the surface coverage, $\tilde{\alpha}_{pol} \equiv \alpha_{pol}/(4\pi a^3) = (\epsilon_p - \epsilon_m)/(\epsilon_p + 2\epsilon_m)$ is the normalized polarizability of a sphere of radius a , $A = (\epsilon_s - \epsilon_m)/(\epsilon_s + \epsilon_m)$ is the strength of the image dipoles defined above, with ϵ_s the permittivity of the substrate. Also,

$$G = \int_0^\infty \frac{\rho^{(2)}(2ax)}{x^2} dx, \quad (12)$$

$$G^I = \int_0^\infty \rho^{(2)}(2ax) \frac{x(x^2 - 2)}{(x^2 + 1)^{5/2}} dx, \quad (13)$$

where $\rho^{(2)(x)}$ is the radial distribution function. Given a reference particle at the origin, this function is proportional to the probability of finding a particle in a spherical shell of radius r and width dr . In a system, like ours, homogeneous and isotropic “on the average”, this function is independent of the location of the reference particle. The expressions given by Eqs. (10) and (11) are adequate for the case of incidence from the monolayer’s side, that is, when the particles in the monolayer are embedded in a material with permittivity ϵ_m and the incident wave comes from that side (external incidence). Note that the presence of the image dipoles in the right hand side of Eqs. (10) and (11) appears in the two terms in the denominators that are multiplied by the quantity A . One is either $A\tilde{\alpha}/8$ or $A\tilde{\alpha}/4$ (depending on the component x or z , respectively), coming from the self-image of the induced dipoles, and the other is the one with the factor AG^I . One can also see that the presence of the self-image remains even in the dilute limit $\Theta\tilde{\alpha}_{pol} \ll 1$.

In case of incidence from the substrate’s side (internal incidence), that is, when the incident wave comes from the medium below the monolayer—assuming obviously a transparent substrate—, and the particles are embedded within the medium above, one can follow the same reasoning as above and conclude that Eqs. (10) and (11) remain valid if one replaces in them $\epsilon_m \leftrightarrow \epsilon_s$ and multiplies the second term in the right hand side of Eq. (11) by ϵ_s/ϵ_m .

For the calculation of the integrals in Eqs. (12) and (13), we choose, $\rho^{(2)}$ as

$$\rho^{(2)}(r) = \begin{cases} 0 & r < 2a \\ 1 & r \geq 2a \end{cases} \quad (14)$$

the so called hole-correlation, that is valid in the dilute regime. This choice assumes that having the reference sphere fixed in a certain location, it cannot be overlapped by another sphere (hard spheres), but the other sphere has otherwise the same probability of being anywhere else. In this case the integrals in Eqs. (12) and (13) can be readily done yielding $G = 1$ and $G^I = \sqrt{2}/4$.

This is a simplifying choice but we have checked that more realistic options yield, essentially, the same results. For example, we have taken the hard-disk radial distribution function reported in [28], for a surface coverage of 0.346, obtaining for the integrals in Eqs. (12) and (13) the values $G = 1.04635$ and $G^I = 0.34067$. Nevertheless, the reflectivity calculations with these values, for this coverage, give results that are indistinguishable from the ones obtained for this same coverage, with the values corresponding to the hole-correlation, that is, $G = 1$ and $G^I = 0.35355$. Thus, we expect that our final results are not sensitive to our simplifying hole-correlation choice.

2.3. Reflection amplitudes

In this section we calculate the expression for the reflection amplitude for both the MGM and the 2D-DM using Fresnel's formulas for a three-layer system. Let us consider first the case of incidence from the substrate side (internal incidence) and consider that the colloidal particles forming the monolayer are spherical with radius a , and randomly located on top of a non-absorptive substrate (medium 1), say glass, with dielectric response ϵ_1 (real), and embedded in a medium (medium 3) with dielectric response ϵ_3 (see Fig. 2). Then one assumes that a plane wave oscillating with frequency ω and wavevector \vec{k}_1 is incident from the substrate side at an angle of incidence θ_1 . If we place the \hat{e}_z axis perpendicular to the monolayer with the origin at the interface between media 1 and 3, one can regard this system as a three-layer system where layer 1 occupies the region $z < 0$, layer 2 the region $0 < z < 2a$ and layer 3 the region $z > 2a$ (see Fig. 2).

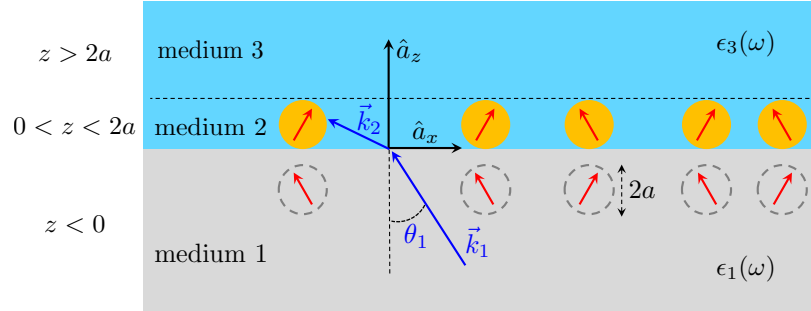


Fig. 2. Schematics of the three-layer system illuminated from the substrate side, internal incidence configuration, with wavevector \vec{k}_1 at an angle of incidence θ_i respect to the normal to the monolayer direction \hat{a}_z .

Now, in order to calculate the reflection amplitude r_{123} , defined as the amplitude of the reflected electric field E_r in medium 1 over the amplitude of the incident field E_i , one simply uses the Fresnel's formula for a three-layer system (see for example [26]), that is,

$$r_{123} = \frac{r_{12} + r_{23} \exp[2ik_{2z}d]}{1 + r_{12}r_{23} \exp[2ik_{2z}d]}, \quad (15)$$

where $d = 2a$ and r_{12} and r_{23} are the reflection amplitudes for the interface between media 1 and 2 and between media 2 and 3, respectively, and k_{2z} is the z component of the wavevector of the electromagnetic wave in layer 2.

2.3.1. Maxwell Garnett model

In the MGM the colloidal monolayer is usually replaced by a film of thickness $2a$ —a not firmly justified choice—(medium 2, see Fig. 2) with an effective dielectric response, which we denote by ϵ_2 and it is given by ϵ_{MG}^{eff} in Eq. (1).

The Fresnel's reflection amplitudes for interfaces between media i and j are given by

$$r_{ij}^s = \frac{k_{iz} - k_{jz}}{k_{iz} + k_{jz}} \quad \text{and} \quad r_{ij}^p = \frac{\epsilon_j k_{iz} - \epsilon_i k_{jz}}{\epsilon_j k_{iz} + \epsilon_i k_{jz}}, \quad (16)$$

where the superscripts in r_{ij} denote s or p polarization. Here k_{iz} ($i = 1, 2, 3$) denotes the z component of the wavevector given by the corresponding dispersion relation in medium i ($i = 1, 2, 3$) and given by

$$k_{iz} = k_0 \sqrt{\tilde{\epsilon}_i - \tilde{\epsilon}_1 \sin^2 \theta_1}, \quad i = 1, 2, 3, \quad (17)$$

where k_0 is the wavevector in vacuum, $\tilde{\epsilon}_i = \epsilon_i/\epsilon_0$, $\tilde{\epsilon}_1 = \epsilon_1/\epsilon_0$ and θ_1 is the angle between \vec{k}_1 and \hat{e}_z . To calculate r_{123} for a given polarization, one simply substitutes in Eq. (15) the corresponding r_{ij} .

2.3.2. 2D dipole model

The calculation of the reflection amplitudes for incidence from the substrate side, in the 2D-DM, follows a very similar procedure as the one described above for the MGM. The objective is the calculation of r_{123} and one uses the same formula given in Eq. (15). The only difference is that in the 2D-DM the effective permittivity of the monolayer, medium 2, has a tensorial character $\overleftrightarrow{\epsilon}_2 = \text{diag}(\epsilon_{xx}^{\text{eff}}, \epsilon_{xx}^{\text{eff}}, \epsilon_{zz}^{\text{eff}})$, where $\epsilon_{xx}^{\text{eff}}$ and $\epsilon_{zz}^{\text{eff}}$ are given by Eqs. (10) and (11), and for the choice of a hole-correlation as the radial distribution function [Eq. (14)], they can be written as

$$\frac{\epsilon_{xx}^{\text{eff}}}{\epsilon_3} = 1 + \frac{2\Theta\tilde{\alpha}_{pol}}{1 - A\frac{\tilde{\alpha}_{pol}}{8} - \Theta\tilde{\alpha}_{pol}\frac{1}{2}\left(1 - A\frac{\sqrt{2}}{4}\right)}, \quad (18)$$

$$\frac{\epsilon_3}{\epsilon_{zz}^{\text{eff}}} = 1 - \frac{2\Theta\tilde{\alpha}_{pol}}{1 - A\frac{\tilde{\alpha}_{pol}}{4} + \Theta\tilde{\alpha}_{pol}\left(1 + A\frac{\sqrt{2}}{4}\right)} \frac{\epsilon_3}{\epsilon_1}, \quad (19)$$

where $\tilde{\alpha}_{pol} = (\epsilon_p - \epsilon_3)/(\epsilon_p + 2\epsilon_3)$ and $A = (\epsilon_1 - \epsilon_3)/(\epsilon_1 + \epsilon_3)$.

When the reflection amplitudes r_{12} and r_{23} are calculated taking account the tensorial character of $\overleftrightarrow{\epsilon}_2$ one obtains

$$r_{12}^s = \frac{k_{1z} - k_{2z}^s}{k_{1z} + k_{2z}^s} \quad \text{and} \quad r_{12}^p = \frac{\epsilon_{xx}^{\text{eff}} k_{1z} - \epsilon_1 k_{2z}^p}{\epsilon_{xx}^{\text{eff}} k_{1z} + \epsilon_1 k_{2z}^p}, \quad (20)$$

$$r_{23}^s = \frac{k_{2z}^s - k_{3z}}{k_{2z}^s + k_{3z}} \quad \text{and} \quad r_{23}^p = \frac{\epsilon_3 k_{2z}^p - \epsilon_{xx}^{\text{eff}} k_{3z}}{\epsilon_3 k_{2z}^p + \epsilon_{xx}^{\text{eff}} k_{3z}}, \quad (21)$$

where $k_{2z}^s = k_0 \sqrt{\epsilon_{xx}^{\text{eff}} - \tilde{\epsilon}_1 \sin^2 \theta_1}$ and $k_{2z}^p = k_0 \sqrt{\epsilon_{xx}^{\text{eff}} - \gamma \tilde{\epsilon}_1 \sin^2 \theta_1}$. Here γ is the anisotropy factor defined as $\gamma \equiv \epsilon_{xx}^{\text{eff}}/\epsilon_{zz}^{\text{eff}}$ and $\tilde{\epsilon}_{xx}^{\text{eff}} = \epsilon_{xx}^{\text{eff}}/\epsilon_0$. Finally, to calculate r_{123} for a given polarization (s or p), one substitutes in Eq. (15) the corresponding values of r_{12} , r_{23} and k_{2z} given in Eqs. (18)-(21).

3. Multiple-scattering approach

If particles in a disordered monolayer are not small compared to the wavelength of the incident light, one cannot approximate the field scattered by any of the particles as that radiated by an oscillating electric dipole. In general, higher order multipoles are induced in the particles and the mathematical complexity for solving the multiple-scattering equations increases considerably [29].

As the scattering efficiency of the particles in a monolayer increases, the so-called fluctuating (diffuse) component of light becomes important. But let us recall, that the total field in the presence of the monolayer can be split into an average (coherent) component, that travels in a well-defined directions, and a fluctuating (diffuse) component, that travels in all different directions. Here we will restrict our attention to the reflection and transmission of only the coherent component, and with this restriction one is able to define, in the usual way, reflection and transmission amplitudes or coefficients, that are referred to as coherent. If one considers monolayers with low surface coverage it is then possible to make valid approximations that lead to simple expressions of considerable value in many applications.

In fact, for dilute monolayers of spherical particles of arbitrary size, the strategy is to calculate first the coherent reflection and transmission coefficients for a free standing monolayer, and then introduce the substrate by taking into account multiple reflections of the coherent field between the substrate's interface and the monolayer of particles. In this way one eludes dealing with the explicit contribution of the *image* particles which is mathematically cumbersome when particles are not small enough. This strategy is consistent with the effective-field approximation, in which particles are assumed to be excited by the average field, an approximation valid for a low volume density of scatterers. In other words, the local field and the average field are assumed to be approximately equal, and this takes into account multiple-scattering effects, although in a rather limited way.

Following the above-mentioned strategy and assumptions, a multiple-scattering model was developed few years ago for the coherent reflection and transmission of light from a disordered monolayer of identical spheres [21]. By coherent reflection and transmission coefficient we mean the reflection and transmission coefficients of the coherent wave, and by coherent wave we mean the configurational average of the electromagnetic waves. We refer to this model as the coherent scattering model (CSM) starting from rigorous multiple-scattering theory. In [21], a formal and lengthy derivation of the reflection and transmission coefficients for this model was given. For future reference, here we present a simpler but heuristic derivation of the same formulas obtained in [21].

3.1. A simple derivation of the CSM for a free standing monolayer

Let us suppose a plane wave incident into a dilute ensemble of identical spherical particles of radius a and electric permittivity ϵ_p , whose centers are randomly distributed in space within a slab of thickness d . Let us assume the lateral dimensions of the slab are very large compared to the size of the particles and wavelength of radiation, and define the volume filling fraction f as the ratio of the volume occupied by all the particles divided by the volume of the slab. By taking the limit $d \rightarrow 0$, the system becomes a random monolayer of particles as discussed above. Let us assume a plane wave is incident to the slab of particles and place our coordinate system as shown in Fig. 3.

Within the Single Scattering Approximation (SSA), the coherent reflected and transmitted waves, outside the region of space occupied by the particles, are given by [30]

$$\langle \vec{E}_{scat}^t \rangle = -\vec{E}_0 \alpha S(0), \quad (22)$$

$$\langle \vec{E}_{scat}^r \rangle = -\vec{E}_0 \alpha \frac{\sin(k_z^i d)}{k_z^i d} S_n(\pi - 2\theta_i), \quad (23)$$

where $\langle \dots \rangle$ means weighted average over all allowed configurations, \vec{E}_0 is the vector amplitude of the incident electric wave, k_z^i is the z component of the incident wavevector, θ_i is the angle of incidence, $n = 1$ or 2 for either s or p polarization, $S_1(\theta)$ and $S_2(\theta)$ are the diagonal elements of the amplitude scattering matrix of an isolated spherical particle embedded in the matrix, as defined

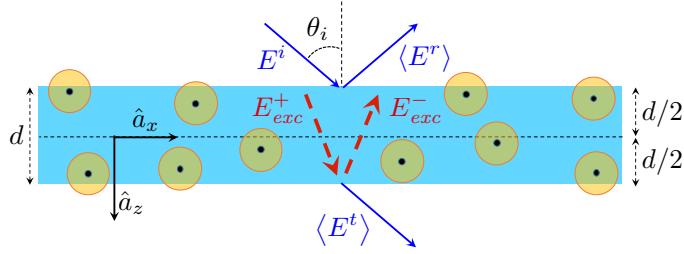


Fig. 3. Schematic illustration of a plane wave incident on a random slab of particles of thickness d . The centers of the particles are restricted to lie within the slab. The dashed line indicates the plane that divides the slab in two equal halves. On the average, half of the particles are in the upper slab and half on the lower slab. The origin of coordinates is placed on the plane at the middle of the slab and the z axis points towards the transmission hemisphere.

in [31], and $S(0) \equiv S_1(\theta = 0) = S_2(\theta = 0)$ is the so-called forward scattering amplitude. The functions $S_1(\theta)$ and $S_2(\theta)$ can be calculated using the Mie solution of the scattering problem [31]. The factor α is given by

$$\alpha = \frac{k_m d}{\cos \theta_i} \frac{3f}{2x_m^3}, \quad (24)$$

where $k_m = k_0 n_m$ is the wavenumber of light in the medium surrounding the particles (the matrix) and $x_m = k_m a$ is the so-called size parameter. The coherent reflection coefficient of a disordered and dilute monolayer of particles in the SSA is obtained by dividing the coherently-scattered field in the reflection hemisphere, by the amplitude of the incident wave; whereas the coherent transmission coefficient is obtained by adding the incident wave and the coherently scattered field in the transmission hemisphere, and then dividing by the amplitude of the incident wave. Then one takes the limit $d \rightarrow 0$ and obtains

$$t_{coh} = 1 - \alpha S(0), \quad (25)$$

$$r_{coh} = -\alpha S_n(\pi - 2\theta_i). \quad (26)$$

In the limit $d \rightarrow 0$ one can write that the volume filling fraction $f = (4a)/(3d)\Theta$, where Θ is the surface coverage by the particles $(2N\pi a)/A$. Then α can be written as

$$\alpha = \frac{2\Theta}{x_m^2 \cos \theta_i}, \quad (27)$$

where $\Theta = N(\pi a^2)/A$ is the surface coverage.

Clearly, both coefficients in the SSA, Eqs. (25) and (26), diverge as the angle of incidence approaches grazing, because $\alpha \rightarrow \infty$ when $\theta_i \rightarrow \pi/2$. This means that the SSA is limited to small angles of incidence. Also, the transmission coefficient in the SSA is flawed even in the dilute limit since its magnitude square can be larger than unity when particles are small compared to the wavelength [21, 32].

To correct the flaws of the SSA we must take into account the contributions of at least some multiple-scattering effects on the calculation of the field exciting the particles. We can do this on an average way, by dividing artificially the space occupied by the slab of particles, in two thinner slabs and solving self-consistently for the average field on the plane between them. In this way, any given particle will be illuminated on the average by the fields scattered by all other particles, in addition to the incident field.

To this end we assume that in-between the half-slabs the average wave consists of two plane waves. One traveling in the direction of incidence, and the other one traveling in the specular direction, as shown in Fig. 3. We then write the field exciting the particles, as

$$\vec{E}_{exc} = E_{exc}^+ \exp[i \vec{k}^i \cdot \vec{r}] \hat{e}_i + E_{exc}^- \exp[i \vec{k}^r \cdot \vec{r}] \hat{e}_r, \quad (28)$$

where $\vec{k}^i = k_m \sin \theta_i \hat{a}_x + k_m \cos \theta_i \hat{a}_z$, $\vec{k}^r = k_m \sin \theta_i \hat{a}_x - k_m \cos \theta_i \hat{a}_z$, where \hat{a} are the unit vectors along the corresponding cartesian axes, and the unit vectors \hat{e}_i and \hat{e}_r are the polarization vectors of the incident and specularly reflected waves, respectively. These can be for either s or p polarization. If we assume that both halves of the slab of particles (each of thickness $d/2$) are excited by these two waves, then we may calculate the average scattered fields at the plane in-between the half-slabs (the plane $z = 0$) and require self-consistency as clarified below.

To calculate the average fields at any point in space we must sum the incident field plus the average of the fields radiated by all the particles in the whole slab. Ignoring now the actual size of the particles, and assuming these are point Mie scatterers, the radiated fields can be readily calculated at any point in space within the slab of particles (except within the point particles). This is done by assuming that independently of the location of the spheres, there are only two directions in which the scattered fields interfere constructively, thus the two exciting plane waves in Eq. (28) are, on the average, the only fields incident on any of the particles. We then use the formulas derived for the SSA, Eqs. (25) and (26), for each of the two half-slabs. We also consider the particles as point particles, which can be done if the system is dilute [30, 33]. This is equivalent to disregard the statistical correlation between the position of the particles due to their finite size and for this reason the radial distribution function does not appear in the final formulas.

At the plane $z = 0$ (see Fig. 3) the average field traveling in the direction of incidence, \vec{E}_{exc}^+ , is given by the incident field plus the fields radiated by the upper half-slab in the direction of incidence. These latter radiated fields can be calculated as those that would be transmitted and reflected from the upper half-slab of particles ($-\frac{d}{2} < z < 0$), in the single-scattering approximation, as if a plane wave $\vec{E}_{exc}^+ \exp[i \vec{k}^i \cdot \vec{r}] \hat{e}_i$ were incident from above and a plane wave $\vec{E}_{exc}^- \exp[i \vec{k}^r \cdot \vec{r}] \hat{e}_r$ were incident from below. Similarly, we calculate the average field traveling in the specular direction, \vec{E}_{exc}^- , at $z = 0$ as the fields that would be transmitted and reflected from the lower half-slab of particles ($0 < z < \frac{d}{2}$) in the single-scattering approximation, as if a plane wave $\vec{E}_{exc}^+ \exp[i \vec{k}^i \cdot \vec{r}] \hat{e}_i$ were incident from above and a plane wave $\vec{E}_{exc}^- \exp[i \vec{k}^r \cdot \vec{r}] \hat{e}_r$ were incident from below. We now require the average field at $z = 0$ to be equal to the exciting field. This is the so-called effective-field approximation [34]. We then get the following consistency equations:

$$\vec{E}_{exc}^+ \exp[i \vec{k}^i \cdot \vec{r}] \hat{a}_i = \left[E_0 - \frac{1}{2} \alpha S(0) E_{exc}^+ - \frac{1}{2} \alpha S_n(\pi - 2\theta_i) E_{exc}^- \right] \exp[i \vec{k}^i \cdot \vec{r}] \hat{e}_i \quad (29)$$

and

$$\vec{E}_{exc}^- \exp[i \vec{k}^r \cdot \vec{r}] \hat{a}_r = \left[-\frac{1}{2} \alpha S_n(\pi - 2\theta_i) E_{exc}^+ - \frac{1}{2} \alpha S(0) E_{exc}^- \right] \exp[i \vec{k}^r \cdot \vec{r}] \hat{e}_r, \quad (30)$$

where the factor $1/2$ multiplying α is because the thickness of the upper and lower slabs is half that of the full slab (and thus, on the average, half of the particles belong to one slab and the other half belong to the other slab). In deriving Eqs. (29) and (30) we used the fact that a plane wave traveling in the incidence direction, when reflected by a slab of particles, changes its polarization from \hat{e}_i to \hat{e}_r , and a plane wave, when traveling in the specular direction, when reflected, changes its polarization vector from \hat{e}_r to \hat{e}_i . Solving Eqs. (29) and (30) yields

$$\vec{E}_{exc}^+ = \frac{1 + \frac{1}{2} \alpha S_n(0)}{1 + \alpha S(0) + \frac{1}{4} \alpha^2 [S^2(0) - S_n^2(\pi - 2\theta_i)]} E_0 \quad (31)$$

and

$$\vec{E}_{exc}^- = \frac{-\frac{1}{2}\alpha S_n(\pi - 2\theta_i)}{1 + \alpha S(0) + \frac{1}{4}\alpha^2 [S^2(0) - S_n^2(\pi - 2\theta_i)]} E_0. \quad (32)$$

To calculate the reflection and transmission coefficients of the average wave, the so-called coherent reflection and transmission coefficients, we need to calculate the average fields outside the slab of particles. We must sum the incident field and the average radiated fields (or equivalently scattered fields). These can be readily calculated assuming that the two plane waves given in Eqs. (29) and (30) are exciting all the particles in the whole slab of particles of thickness d and using the formulas derived for the SSA, Eqs. (25) and (26). The total transmitted and reflected average fields are obtained as

$$\vec{E}_{coh}^t = \vec{E}^i + \left\langle \vec{E}_{scat}^t(z > \frac{d}{2}) \right\rangle \quad (33)$$

$$= \left[E_0 - E_{exc}^+ \frac{\alpha}{\cos \theta_i} S(0) - E_{exc}^- \frac{\alpha}{\cos \theta_i} S_n(\pi - 2\theta_i) \right] \exp[i \vec{k}^i \cdot \vec{r}] \hat{e}_i, \quad (34)$$

$$\vec{E}_{coh}^r = \left\langle \vec{E}_{scat}^r(z < -\frac{d}{2}) \right\rangle \quad (35)$$

$$= \left[-E_{exc}^+ \frac{\alpha}{\cos \theta_i} S_n(\pi - 2\theta_i) - E_{exc}^- \frac{\alpha}{\cos \theta_i} S(0) \right] \exp[i \vec{k}^r \cdot \vec{r}] \hat{e}_r, \quad (36)$$

where $n = 1$ or 2 for s or p polarization and we used the SSA formulas, Eqs. (25) and (26), assuming $k_z^i d \ll 1$. The coherent reflection and transmission coefficients are given by $r_{coh} = E_{coh}^r/E_0$ and $t_{coh} = E_{coh}^t/E_0$.

Now we can take the limit $d \rightarrow 0$ and α takes the form given in Eq. (27). Then, the coherent reflection and transmission coefficients for a monolayer of particles are given by

$$r_{coh} = \frac{-\alpha S_n(\pi - 2\theta_i)}{1 + \alpha S(0) + \frac{1}{4}\alpha^2 [S^2(0) - S_n^2(\pi - 2\theta_i)]} \quad (37)$$

and

$$t_{coh} = \frac{1 - \frac{1}{4}\alpha^2 [S^2(0) - S_n^2(\pi - 2\theta_i)]}{1 + \alpha S(0) + \frac{1}{4}\alpha^2 [S^2(0) - S_n^2(\pi - 2\theta_i)]}. \quad (38)$$

These coefficients are expected to be accurate only in the dilute limit but for arbitrary particle size and angle of incidence.

3.2. Introducing the substrate

Now let us suppose the particles are located on a flat interface between two media, namely, medium 1 and medium 3 (see Fig. 2). Within the same approximations already made to derive the coherent reflection and transmission coefficients, we can see the monolayer as an effective surface (i.e., an infinitely thin slab) with reflection and transmission coefficients given by Eqs. (37) and (38) and located one particle radius a away from the interface. Then we can calculate the multiple reflections between the monolayer's effective plane and the interface between medium 1 and 3. Since the radius of the particles can be comparable or larger than the wavelength of radiation we should take into account the phase delay of the average wave as it travels between the interface and the monolayer's effective surface. There are two different cases one can consider. Namely, the particles can be on the side of incidence or they can be on the transmission side. That is, viewing the system from the incidence side, the particles can be before or after the interface.

If particles are located before the interface, we get [21],

$$r(\theta_i) = r_{\text{coh}}(\theta_i) + \frac{r_{13}(\theta_i) t_{\text{coh}}^2(\theta_i) \exp[i\beta_1]}{1 - r_{13}(\theta_i) r_{\text{coh}}(\theta_i) \exp[i\beta_1]}, \quad (39)$$

where $\beta_1 = 2k_0 a n_1 \cos \theta_i$ and $r_{13}(\theta_i)$ is the Fresnel reflection coefficient of the interface between medium 1 and 3 for the corresponding polarization (either *s* or *p*). In the latter formula $r_{\text{coh}}(\theta_i)$ and $t_{\text{coh}}(\theta_i)$ should be calculated for a monolayer of particles embedded in a medium of refractive index n_1 .

If particles are located after the interface, then the incident wave gets refracted at the interface according with Snell's law and illuminates the particles at an angle

$$\theta_t = \arcsin\left(\frac{n_1}{n_2} \sin \theta_i\right). \quad (40)$$

Then we obtain [21]

$$r(\theta_i) = \frac{r_{13}(\theta_i) + r_{\text{coh}}(\theta_t) \exp[i\beta_2]}{1 + r_{13}(\theta_i) r_{\text{coh}}(\theta_t) \exp[i\beta_2]}, \quad (41)$$

where $\beta_2 = 2k_0 a n_3 \cos \theta_t$ and $r_{\text{coh}}(\theta_t)$ should be calculated for a monolayer of particles embedded in a refractive index n_3 .

Equations (39) and (41) do not take into account possible local corrections to the exciting fields on the particles due to their proximity to the substrate's interface. These corrections may be important at low angles of incidence and for very large particles (see Ref. [35]). Nevertheless Eq. (37) through (41) were extended to polydisperse system of particles in [36] and used to compare theoretical calculations with experimental curves of the reflectivity and transmissivity of a flat interface covered by a polydisperse monolayer of highly scattering particles. The comparison showed a very good agreement even for moderately dense monolayers, despite the model was derived from approximations valid only in the dilute limit.

4. Comparison between models: CSM, MGM and 2D-DM

In this section we present calculations of the coherent reflectance of a surface covered by a disordered monolayer of spherical particles using the three models reviewed in the previous sections: the Coherent Scattering Model (CSM), the 2D-dipole model (2D-DM) and the Maxwell Garnett thin film model (MGM). For comparison purposes we include, in addition, graphs of the reflectivity of a surface covered by a thin homogenous film (ThF) of the same material of which the particles forming the monolayer are made of, and with a thickness such that it has the same volume of material as the particles in the monolayer. Here we will refer to the coherent reflectance also as the reflectivity [37].

For all our examples here we chose gold [38] as the particles' material since it exhibit the effects of the surface plasmon resonance, which is currently of interest in many applications [39,40]. We also assumed *p* polarized light (TM polarization), since we demonstrated recently, in reflectance experiments [13,25], that in this polarization one obtains the best sensitivity for the detection and characterization of particles forming the monolayer.

For all the following figures presented in this section, except in the last one (Fig. 10), the particles are assumed to be adsorbed on a glass-air interface. The refractive index of air was taken as 1 for all wavelengths considered and the refractive index of glass was assumed to that of BK7 glass [41] (a common glass used in many optical elements). We present graphs of the reflectivity for two different configurations: one in which the particles are in front of the interface and the incidence medium is air (external-incidence configuration); and another one in which the particles are behind the interface and the incidence medium is glass (internal-incidence configuration).

We plot the reflectivity versus, either the angle of incidence, the wavelength of the incident radiation, the particles' radii or the surface coverage, for fixed values of all other parameters. The purpose of comparing the reflectivity predicted by each model is two-fold. On the one hand, if all of them were derived on soundly physical grounds, they should coincide at least qualitatively (for small spherical particles and in the dilute limit), and verifying this should endorse their assertive use in different applications. On the other hand, when the particles are not small enough to be modelled as induced dipoles or when the surface coverage is not small compared to one, the different models should deviate from each other, and thus we should obtain a rough idea of the validity of each model. In all our graphs we also include the reflectivity of the bare interface as a reference in order to perceive the effect on the particles of the reflectivity of the surface.

In Fig. 4, we plot the reflectivity of an air-glass interface covered by a disordered monolayer with a 5% surface coverage and at a wavelength of 540 nm, which is close to the dipolar plasmon resonance of the spherical gold particles, for both internal and external configurations, left and right columns in Fig. 4, respectively. We also considered two different radius of the identical nanoparticles forming the monolayer: 10 nm and 30 nm, corresponding to the top and bottom rows in Fig. 4, respectively. We are aware that 30 nm might be too big for the models that consider only a dipolar component of the induced charge; nevertheless, here we want to explore how far can we go in particle size and still obtain reasonable results, when compared with a model that takes the full multipolar contributions. At first glance, we appreciate that the effect of the nanoparticles is noticeable only in an internal-reflection configuration and behind the critical angle (about 41° angle of incidence), see Fig. 4(a) and 4(c), a fact that we highlighted in previous published work [13, 25]. In this case, if we remove the particles from the interface we would have a total internal reflection, and thus this situation may be referred as frustrated total internal reflection. All models considered deviate from each other, although qualitatively the CSM, the 2D-DM and the MGM have the same behavior. The ThF curve has a different curvature just behind the critical angle, thus having a different qualitative behavior, see Fig. 4(a) and 4(c). In an external reflection configuration [Fig. 4(b) and 4(d)], we see that the effect of the particles is hardly detectable for this surface coverage.

In Fig. 5 we plot the calculated reflectivity spectra for the different models with the same parameters as for Fig. 4, i.e., surface coverage of 5%, both internal (left column) and external (right column) configurations, two particle radii, 10 nm (top row) and 30 nm (bottom row), but in this case at normal incidence ($\theta_i = 0$). The general trend for all cases in Fig. 5 is that the CSM, the 2D-DM and the MGM, have the same qualitative behavior, whereas the ThF calculation is qualitatively very different. For the internal configuration, in Fig. 5(a) and 5(c), it is interesting to note that the dipolar surface plasmon resonance is seen as a dip in the reflectivity spectra at around 520 nm, while for the external configuration, Fig. 5(b) and 5(d), is seen as a peak with a slight blue shift compared with the dip for internal configuration. It is also interesting that the reflectivity is generally *below* that of the bare surface except for a wavelength range around the surface plasmon resonance in an external reflection configuration, and only for the smaller particle radius of 10 nm. In fact the shape of the curves in an external reflection configuration is qualitatively very different for particles of 10 nm radii than for particles with 30 nm radii. This can be understood considering that small nanoparticles basically scatters light isotropically while large particles scatters light predominately towards the incidence direction, called forward scattering. So, one will expect a higher reflectivity coming from a monolayer of small nanoparticles than from a monolayer with larger ones. Nevertheless, in all cases the three monolayer models considered, (CSM, 2D-DM and MGM) predict basically the same reflectivity curves, and differ drastically from the thin-film model.

In Fig. 6 we plot the reflectivity spectra for the same parameters and configurations as in Fig. 5 (i.e., surface coverage of 5% and particles of radii of 10 nm and 30 nm), but for an angle of incidence of $\theta_i = 45^\circ$, which is larger than the critical angle of the glass-air interface, thus

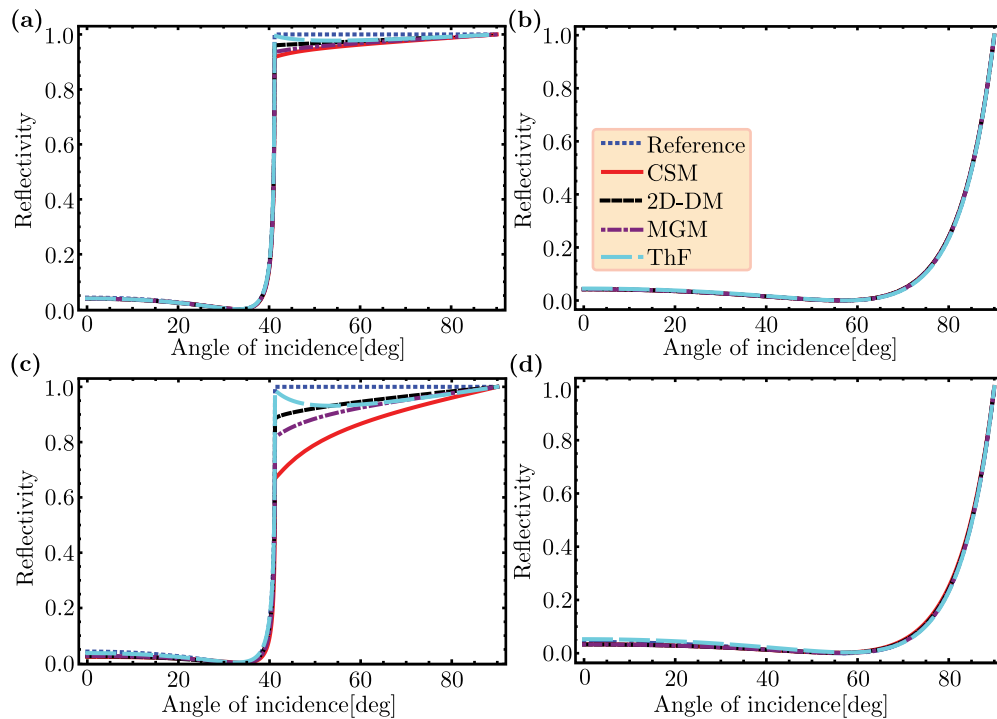


Fig. 4. Reflectivity as a function of the angle of incidence θ_i for fixed wavelength of 540 nm and surface coverage of 5%, for p (TM) polarization, and two different radius of the nanoparticles forming the monolayer and for both configurations: internal configuration for a radius of (a) 10 nm and (c) 30 nm, and external configuration for a radius of (b) 10 nm and (d) 30 nm. Inset in (b) applies to all the plots in this figure.

this case corresponds to frustrated total internal reflection. In this case, it is evident that the effect of the nanoparticles forming the monolayer, on the absolute value of the reflectance, is stronger for a total internal-reflection configuration, Fig. 6(a) and 6(c), than for the external configuration, Fig. 6(b) and 6(d). Qualitatively, the three monolayer models predict the same behavior but, quantitatively they deviate from each other noticeably. Particularly, in an internal reflection configuration and around the dipolar surface plasmon resonance wavelength (around 520 nm) and smaller wavelengths, the difference between the models is magnified. Also, note that the CSM model decays more steeply as the wavelength decreases than the other two models. The reason is that for the smaller wavelength the relative size of the particles compared to the wavelengths is larger and scattering becomes more important. In these examples the ThF calculations are completely off those with the three monolayer models. In particular, in an external reflection configuration the ThF calculations predict a reflectivity above that of the bare substrate whereas the three monolayer models predict a reflectivity below that of the substrate, for all the wavelengths considered in the graphs.

To inspect the behavior of the three models with the size of the nanoparticles forming the monolayer, we plot the reflectivity versus the radius of the particles in Fig. 7, at a fixed wavelength of 540 nm and maintaining a constant surface coverage fraction of 5%. This means that the number density of particles increases as the particle radius decreases. In general, one can see that as the particles radii tend to zero the reflectivity tends to that of the bare surface for all models.

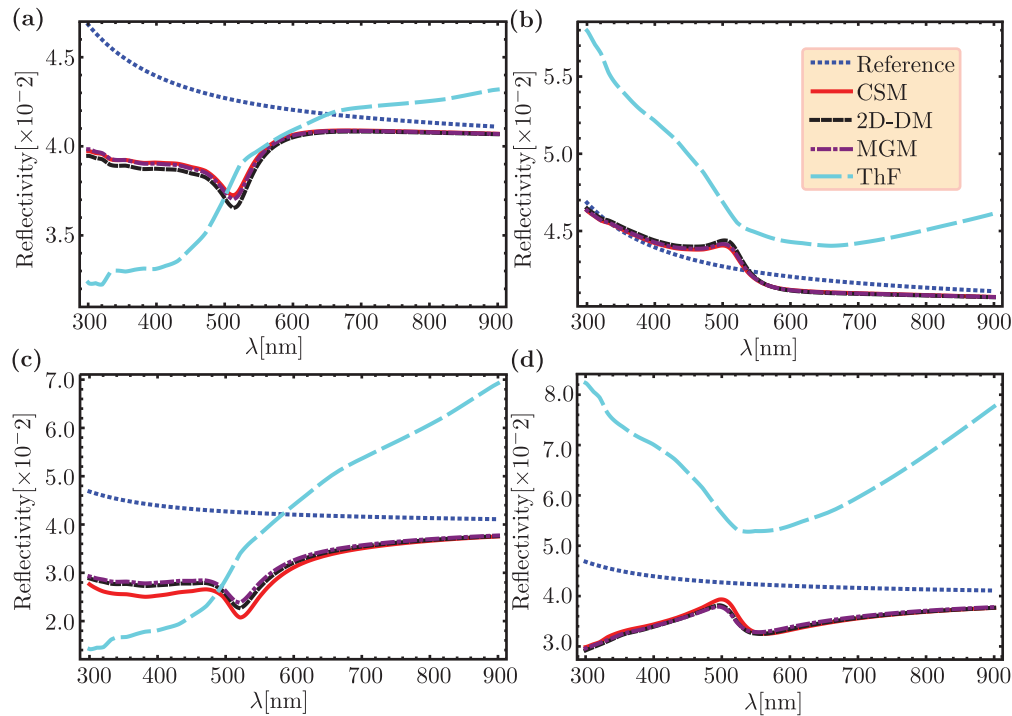


Fig. 5. Reflectivity spectra for normal incidence and surface coverage of 5%, for two different radius of the nanoparticles forming the monolayer and for both configurations: internal configuration for a radius of (a) 10 nm and (c) 30 nm, and external configuration for a radius of (b) 10 nm and (d) 30 nm. Inset in (b) applies to all the plots in this figure.

The CSM deviates strongly from the 2D-DM and the MGM calculations as the particle radius increases, although for an external-reflection configuration, Fig. 7(b) and 7(d), this happens only for particles with radii larger than about 40 nm, which may be regarded already as large particles. In an internal-reflection configuration and for normal incidence, Fig. 7(a), the CSM deviates clearly for radii larger than 20 nm and for an angle of incidence of 45° , Fig. 7(c), all three models deviate from each other noticeably right from the beginning. In an external reflection configuration, Fig. 7(b) and 7(d), the ThF calculation is above the reflectivity of the bare substrate whereas those with the models are below, for all particle radii considered.

In Figs. 8 and 9 we plot the reflectivity versus the surface coverage at a fixed wavelength of 540 nm, for particles of radius of 10 nm (Fig. 8) and 30 nm (Fig. 9), for both internal-reflection configuration (left column) and external-reflection configuration (right column), and two angles of incidence: 0° (top row) and 45° (bottom row). We can appreciate that the models deviate from each other strongly for the case of frustrated total internal reflection and less for the other cases considered. The ThF curves are way off those of the monolayer models particularly for the cases where there would be partial surface reflection in the absence of the particles. It is interesting to note in Fig. 8(b) and 8(d), as well as in all the graphs of Fig. 9, that the reflectivity predicted by the monolayer models start decreasing as the surface coverage increases, but at some point the curves reach a minimum and start increasing as the surface coverage increases further, and in some cases it can cross that of the bare substrate [Fig. 8(b) and 8(d)].

In Figs. 4-9 we confirm that the CSM deviates from the 2D-DM and the MGM when the radius

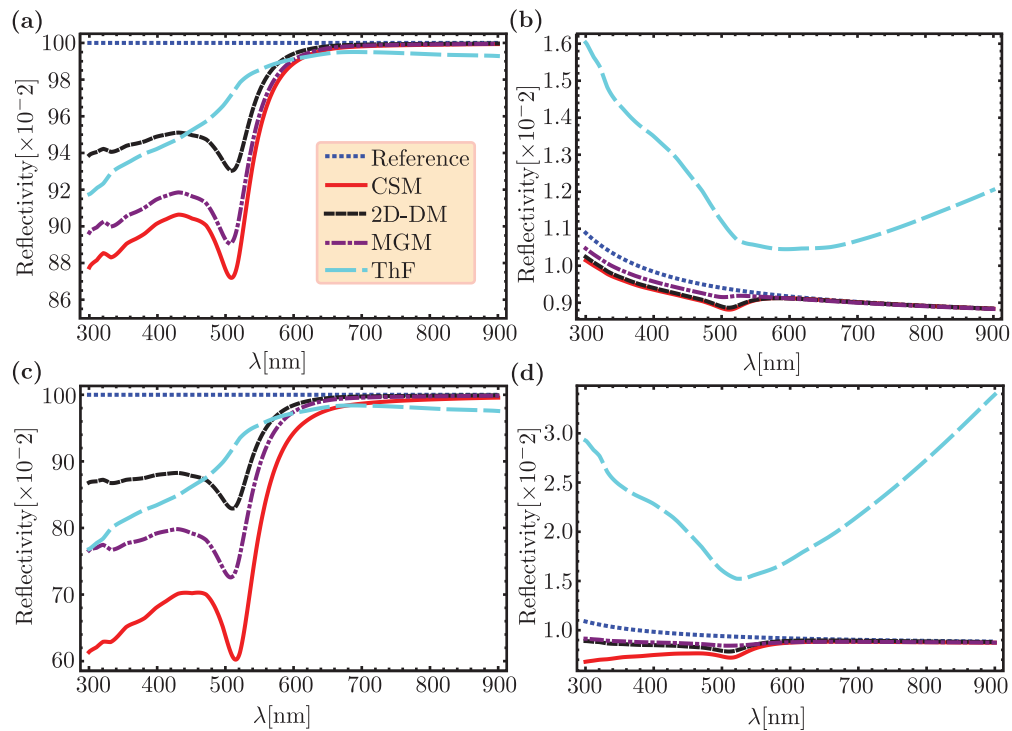


Fig. 6. Reflectivity spectra for an angle of incidence $\theta_i = 45^\circ$ and surface coverage of 5%, for p (TM) polarization, and two different radii of the nanoparticles forming the monolayer and for both configurations: internal-reflection configuration for a radius of (a) 10 nm and (c) 30 nm, and external-reflection configuration for a radius of (b) 10 nm and (d) 30 nm. Inset in (a) applies to all the plots in this figure.

of the nanoparticles forming the monolayer is large. This is expected since the 2D-DM and the MGM consider the particles as induced electric dipoles, whereas the CSM takes into account induced multipoles, both electric and magnetic. Thus, for small surface coverages when the CSM deviates from the other two models, we may assume that the validity of the latter ones is reaching their limits. On the other hand, for small particles, as the surface coverage increases the 2D-DM and the MGM move apart from the CSM. Since the corrections to the local field are better taken in the 2D-DM and the MGM models than in the CSM, one expects the first two models to be valid at moderately high surface coverage, thus this departure indicates that the CSM is reaching its limits of validity. We can also appreciate in Figs. 4-9 that the 2D-DM and the MGM follow each other closely except in the cases of frustrated total internal reflection, where they behave qualitatively similar but deviate quantitatively from each other. This result is rather surprising since, besides some intrinsic differences in the effective electric permittivity in the MGM and the 2D-DM, the former one does not include the effects of the images of the particles. This means that the effects of the images are not strong in the examples considered. From Figs. 4-9 we can see that, in general, the influence of the gold nanoparticles on the surface's reflectance is larger in an internal-reflection configuration than in an external-reflection configuration. If we define the sensitivity as the rate of change of the reflectance with respect to the surface coverage of the particles, we then may say that an internal-reflection configuration is more sensitive to the deposition of nanoparticles than an external-reflection configuration.

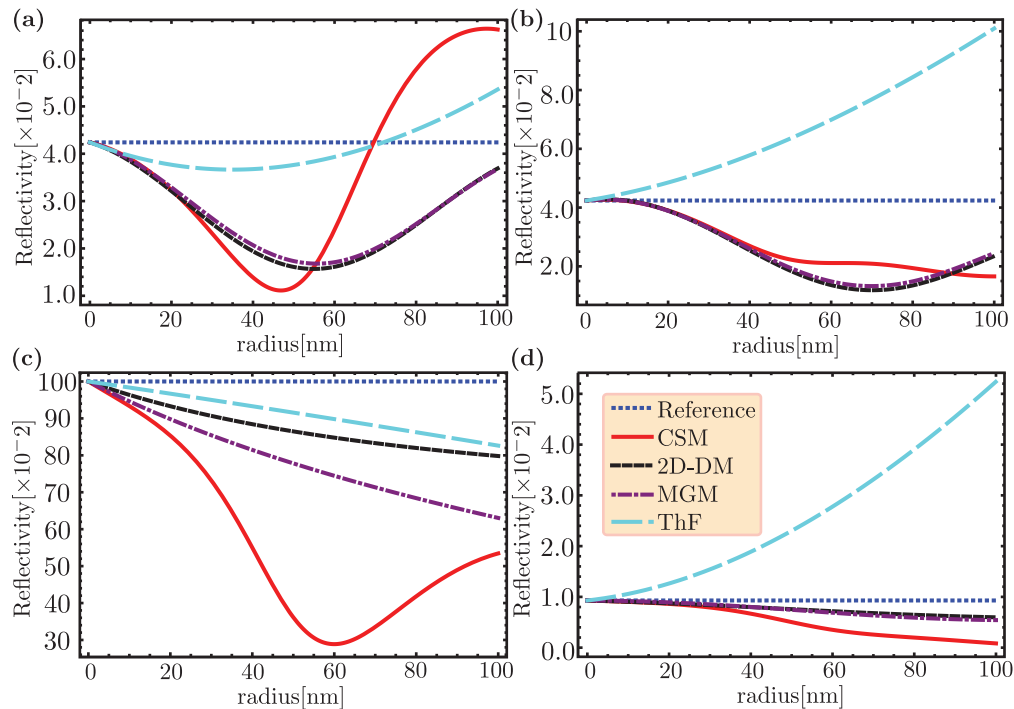


Fig. 7. Reflectivity versus the radius of the particles forming the monolayer, at a fixed wavelength of 540 nm and surface coverage of 5%, for p (TM) polarization, and two different angles of incidence and for both configurations: internal-reflection configuration for an angle of (a) $\theta_i = 0$ and (c) $\theta_i = 45^\circ$, and external-reflection configuration for an angle of (b) $\theta_i = 0$ and (d) $\theta_i = 45^\circ$. Inset in (d) applies to all the plots in this figure.

To exhibit more clearly the effects of the particles' images on the substrate included in the 2D-DM, we consider a highly reflecting substrate, such as a metallic one. In this case only the external-reflection configuration will be physically viable. In Fig. 10 we plot the reflectivity versus the angle of incidence for a monolayer of gold nanoparticles (dielectric function taken from [38]), of 10 nm radius, adsorbed at an air-silver interface (Ag dielectric function taken from [38]). We assume a 10% surface coverage and a wavelength near the dipolar surface plasmon resonance of the particles of around 540 nm. The plots were calculated with the 2D-DM including the particles' images and excluding them. We also include the base substrate's reflectivity for comparison. We can appreciate in Fig. 10 noticeable differences between the calculations with and without the images. Nevertheless, these differences are not very strong and the qualitative behavior of both curves is quite similar. For other substrates considered such as silicon or titanium dioxide (not shown), the differences were basically unnoticeable. We may then conclude that the differences observed in Figs. 4-9 between the 2D-DM and the MGM are due to the 2D geometry and not to the images included in the 2D-DM.

5. Discussion

We can estimate that for small plasmonic particles of radii up to about 20 or 30 nm and a surface coverage up to about 30%, the 2D-DM model with the hole-correlation function is expected to be

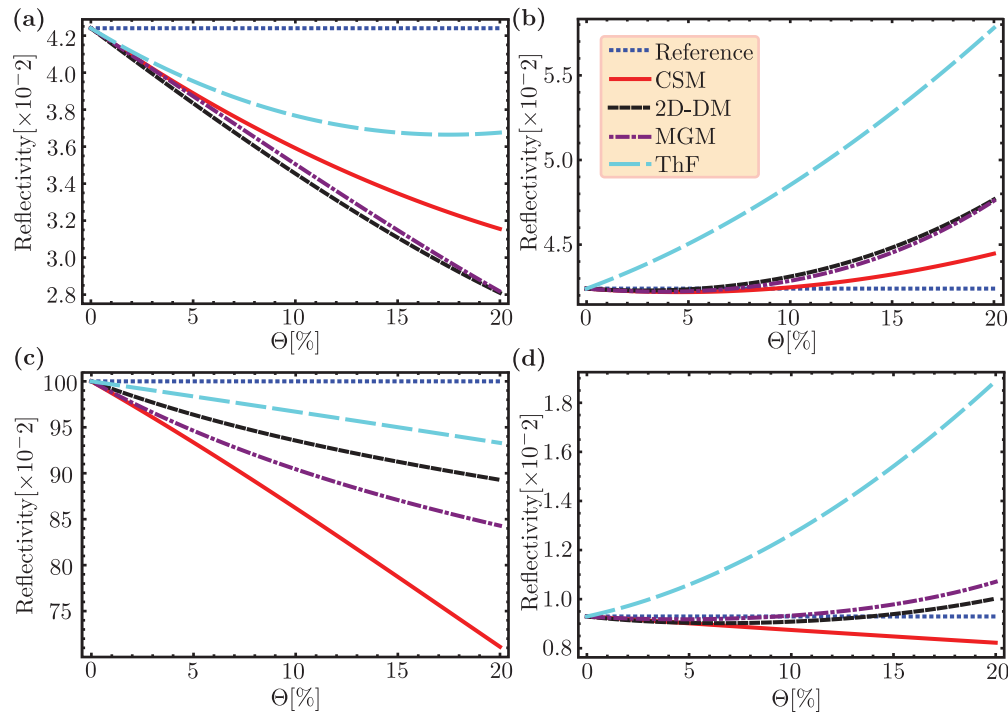


Fig. 8. Reflectivity versus the surface coverage, at a fixed wavelength of 540 nm and radius of the particles forming the monolayer of 10 nm for p (TM) polarization, and two different angles of incidence and for both configurations: internal-reflectance configuration for an angle of (a) $\theta_i = 0$ and (c) $\theta_i = 45^\circ$, and external-reflectance configuration for an angle of (b) $\theta_i = 0$ and (d) $\theta_i = 45^\circ$. Inset in (b) applies to all the plots in this figure.

accurate. For larger particles, the 2D-DM should lose accuracy and the CSM should be a better choice, however, only for smaller surface coverages of about 10% or less. From the comparisons presented above we know now that the MGM should also be accurate in cases where the 2D-DM is expected to be accurate and the substrate is not highly reflective, since both models follow each other closely in these cases. From the figures presented in the previous section we can see that the 2D-DM and the CSM coincide for small particles (less than 25 nm in radius) and small surface coverage (less than 5%). Thus, for smaller particles and smaller surface coverages we can use any of the three models indistinctly.

As already said, to further test the validity of the three models in different scenarios, we could compare their predictions with experimental measurements. A difficult aspect of an experimental test is the fabrication of reproducible samples, with well-characterized particle size and surface coverage over a large enough area, to facilitate experimental measurements of reflectivity at any desired angle of incidence. Assuming such samples are available, from Figs. 4-9 we can identify some attractive configurations to perform experiments, or may be also, “exact” numerical simulations. We can assume that the reflectivity in any case can be measured without much difficulty with an accuracy and precision of 1% or better.

One experimental configuration of interest is the external reflectivity at or about 45° angle of incidence and for particles of 10 nm radius. From Fig. 8 one can see that in this case the 2D-DM and MGM predict a reflectivity larger than that of the bare substrate when the surface coverage

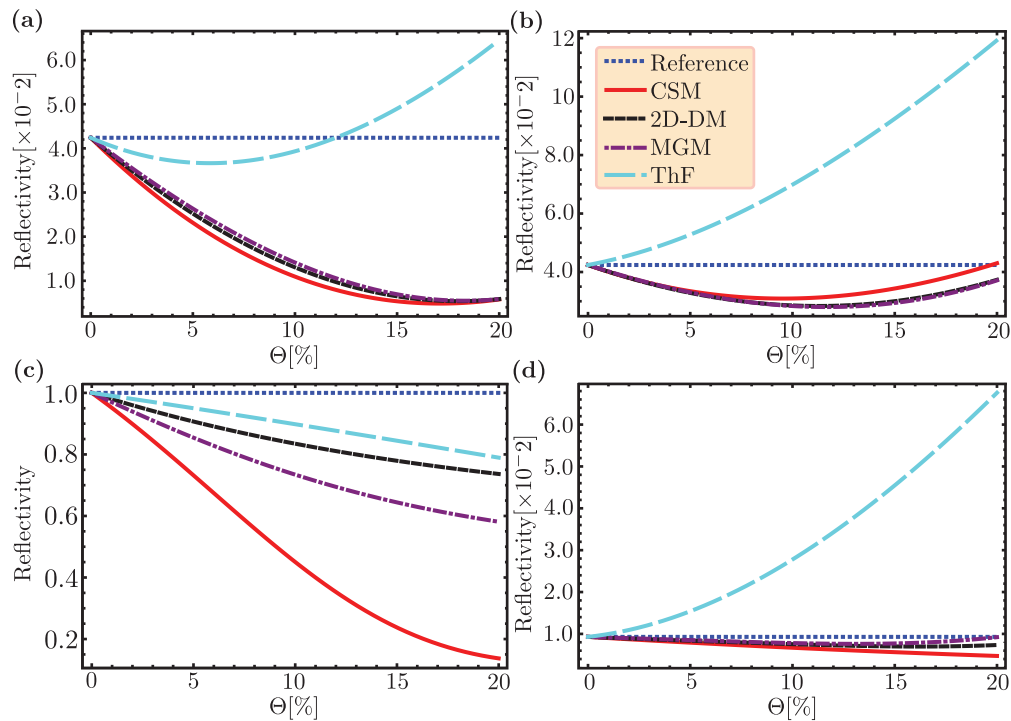


Fig. 9. Reflectivity versus the surface coverage, at a fixed wavelength of 540 nm and radius of the particles forming the monolayer of 30 nm for p (TM) polarization, and two different angles of incidence and for both configurations: internal configuration for an angle of (a) $\theta_i = 0$ and (c) $\theta_i = 45^\circ$, and external configuration for an angle of (b) $\theta_i = 0$ and (d) $\theta_i = 45^\circ$. Inset in (b) applies to all the plots in this figure.

approaches 20%, whereas the CSM predicts a lower reflectivity. 20% of surface coverage is already not “dilute” so one should expect the CSM to be wrong and the 2D-DM and MGM to be right, but an experimental verification is necessary. Also the relative differential reflectivity between the 2D-DM and MGM is large enough to be differentiated in an experimental measurement (about 100%). By relative differential reflectivity we mean the difference in reflectivity of the interface with and without the plasmonic nanoparticles and normalized by the bare substrate’s reflectivity. At this same angle of incidence but for an internal reflection configuration, the divergence in relative differential reflectivity between the three models is large enough to be distinguished experimentally (about 5% between the 2D-DM and MGM and 15% between the MGM and the CSM).

We also propose to measure the reflectivity of a glass interface partially covered by plasmonic monolayer of particles with radii in the range between 80 nm and 100 nm at normal incidence and in an internal reflection configuration. From Fig. 7 one can see that in this case the CSM predicts a reflectivity above that of the substrate whereas the other two models predict a lower reflectivity. In this same configuration but for particles of radii around 60 nm and for an angle of incidence of 45° the differences in reflectivity between the three models are large enough to be measured experimentally (about 10% between the 2D-DM and MGM and 50% between the MGM and the CSM). Additionally, for particles of about 60 nm radius, but now in an external reflection configuration and at 45° angle of incidence, the difference in relative differential reflectivity

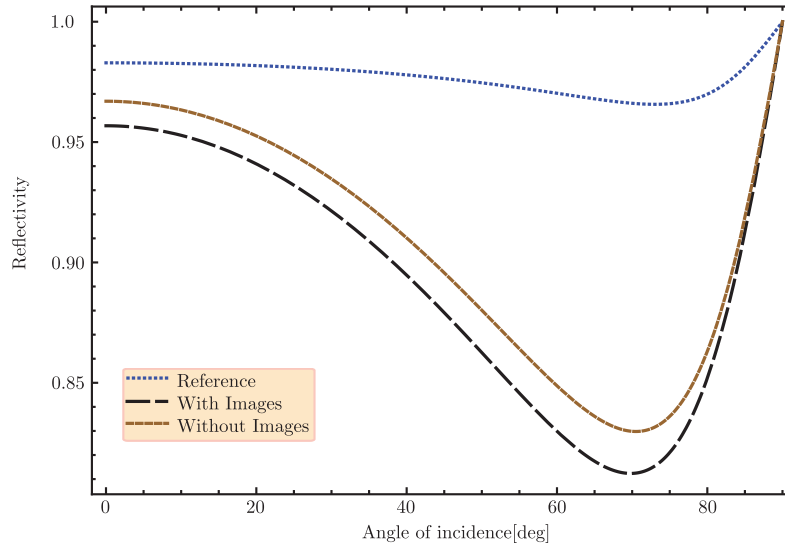


Fig. 10. Reflectivity versus the angle of incidence for a monolayer formed with gold (dielectric function taken from [38]) nanoparticles of 10 nm in radius, embedded in air and supported onto a silver substrate (dielectric function taken from [38]), illuminated with a fixed wavelength of 540 nm and surface coverage of 10%, for p polarization, using the 2D-DM considering images (continuous curve) and without them (long-dashed curve).

between the CSM and the other two models is more than 100% and should be easily measured with an acceptable sample.

By looking at Figs. 4 and 6 we can identify two other attractive experiments to be performed, both with samples of particles of radius between 10 nm and 30 nm. One experiment could be measurements in an internal reflection configuration setup and a 10° range of angles of incidence above the critical angle. In this case [Figs. 4(a) and 4(c)] one can see that the relative differential reflectivity predicted by the three models differ markedly (more than 100% for particles of 30 nm radius). The other experiment can be devised by using the results displayed in Fig. 6(b). In this case we see that the plasmon resonance dip in the spectra at about 510 nm predicted by the MGM for particles of 10 nm in radius and for normal incidence differ noticeably from those predicted by the 2D-DM and CSM.

6. Conclusions

In summary, we showed for p polarization that,

- The CSM, 2D-DM and MGM coincide quantitatively in all cases for gold particles smaller than about 25 nm radius on a glass substrate and surface coverage fractions below 5%. Given that the three models are derived following very different procedures, this is important since it soundly suggests the three models are actually valid in these cases. Thus the reflectivity of a surface partially covered by a disordered monolayer of very small particles can be calculated using any of these models.
- The 2D-DM and the MGM follow each other closely for all surface coverages and particle sizes considered in our examples (gold spherical particles), except behind the critical angle

in an internal reflection configuration.

- c) The changes in reflectivity of light due to the presence of gold nanoparticles at the interface of a glass substrate, is noticeably higher in an internal reflection configuration than in external reflection configuration.
- d) In general, the reflectivity of an equivalent homogenous thin film containing the same amount of material than a particulate monolayer differs strongly from that of the corresponding disordered monolayer. In many cases, for external reflection the thin-film-on-a-substrate reflectivity is higher than that of the bare substrate while that of a monolayer-on-a-substrate is lower.
- e) Some experimental configurations where differences between the predictions of the models are attractive for experimental verification were identified.

The fact that the changes in reflectivity due to the adsorption of nanoparticles is in general larger in an internal rather than an external reflection configuration, is an interesting prediction that could be used advantageously in experiments aiming to detect and characterize nanoparticles on a substrate. Basically, it means that when possible one should choose an internal reflection configuration to obtain reflectance measurements to infer information about the particles.

The analysis presented here for *p*-polarization was also done in parallel for *s*-polarization (not shown in this paper), and in all cases the differences between the models are less noticeable than in *p* polarization. We also performed similar calculations as those presented in Figs. 4-9 (same range of particle sizes and surface coverages) but for lossless dielectric particles of different refractive indices, ranging from 1.4 to 2.8 on an air/glass interface, and found that all three models deviate less from each other than for the examples with gold nanoparticles presented here.

Funding

Dirección General de Asuntos del Personal Académico, Universidad Nacional Autónoma de México (IA105917, IN102218).

Acknowledgments

GML acknowledges scholarship and support from CONACyT, Posgrado de Ingeniería Eléctrica, UNAM. Most of the work performed by OVE on this manuscript was done while he was at Centro de Ciencias Aplicadas y Desarrollo Tecnológico, UNAM.